DIRECT SOUND COMPUTATION OF A FLOW PAST A SQUARE CYLINDER AT LOW MACH AND LOW REYNOLDS NUMBERS

Tiago de Assis Silva, tasilva@mecanica.ufu.br
Fábio G. Temístocles Ferreira, fabiogtf@bol.com.br
Odenir de Almeida, odenir@mecanica.ufu.br
Aristeu da Silveira Neto, aristeus@mecanica.ufu.br

Universidade Federal de Uberlândia
Faculdade de Engenharia Mecânica
Laboratório de Mecânica dos Fluidos - MFlab

Abstract. *The sound generated by a square cylinder placed in a uniform flow at low Mach and low Reynolds numbers has been investigated by direct solution of the two-dimensional unsteady compressible Navier-Stokes equations. The development of a moder digital computer now makes it possible, at least for 2D flows, to simulate a sound field by directly solving the governing equations over the entire range from near to far fields. A computational code has been developed in house to solve the compressible Navier-Stokes equations by using optimized high order numerical schemes. A thirteen points stencil fourth order accurate finite difference schemes was applied for spatial derivatives (with 11, 9 and 7 points at the boundaries). The governing equations was advanced in time by using a fourth order six steps Runge-Kutta method. A set o numerical simulations were performed at Mach numbers 0.1, 0.2 and 0.3, and Reynolds numbers 100, 150 and 200. The time step was $\Delta t = 0.01$ and the total number of grid points were 953×953. Results show that sound waves are generated primarily by vortex shedding form the cylinder surface into its wake. When a vortex is shed from one side of the cylinder, a negative sound wave is generated from that side whereas a positive sound wave is generated from the other side. A dipolar nature of the generated sound is observerd with main propagation direction towards upstream. The frequency of the pressure waves is the same as that of vortex shedding as well as the fluctuation frequency of the lift force. The results also showed that the Mach number has little effect over the generation mechanisms of the sound, but clearly influence the propagation of sound waves to mid and far fields. The Doppler effects is shown to play an important role at finite Mach number. It was observed that when the Reynolds number increase, it is possible to note that the positive and negative sound waves have clearly different propagation angles. This effect has been attributed to significant increase in drag dipole when Reynolds number increases. However this is not a closed explanation and a further invertigation will be necessary to bring a comprehensive understanding for this phenomena.*

Keywords*: computational aeroacoustics, direct sound computation, square cylinder.*

1. INTRODUCTION

The flow around a bluff body is one of the basic subjects in fluid mechanics, because it contains not only fundamentally important problems (such as forces acting on the body, transition to turbulence, acoustic emission, etc.), but also a variety of practical application (such as structural design of buildings, bridges, trains, landing gears, etc.). A square cylinder is one of the typical examples of the bluff body, and a number of studies on the flow around square cylinders has been done both experimentally (Okajima (1982), Knisely (1990), Norberg (1993)) and computationally (Davis and Moore (1982), Sohankar et al (1999), Inoue et al (2006a and b), Inoue and Suzuki (2007)).

It is recognized that the production of the sound is connected with the instability of the vortex sheets in the cylinder wake (Kármán vortex street). It is also known that the frequency of the sound is the same as the shedding frequency of vortices from the cylinder into its wake and the sound emitted is called aeolian tones, Inoue and Hatakeyama (2002). The aeolian tones that are radiated from the flow around a bluff body have also been researched for more than 100 years. A brief review on the aeolian tone has been given by Inoue and Hatakeyama (2002) for the case of a circular cylinder. The aeolian tone that is radiated from the flow around a square cylinder has received far less attention than that from the flow around a circular cylinder, and works from the open literature are rather scarce. From an engineering point of view, aeolian tone that are radiate from the flow around a square cylinder are important; a typical example is the tones generated by landing gears, which has many circular and square cylinders as their structural components.

The development of a modern digital computers now makes it possible, at least for 2D flows, to simulate a sound field by directly solving the compressible Navier-Stokes equations over the entire range from the near to far fields. Inoue and Hatakeyama (2002) investigated the sound generated by a single circular cylinder in a uniform flow at Reynolds number 150 by direct solution of the 2D unsteady compressible Navier-Stokes equations, and clarified the generation and propagation mechanisms of the sound in some detail. Inoue et al (2006a and b), and Inoue et al (2007), extended the work done by Inoue and Hatakeyama (2002) to study the sound generated by a flow around square cylinders in different arrangements and sizes.

RMS or rms means 'Root Mean Square'.

The main purpose of this paper is to study the generation mechanism of the sound that is radiated by the flow past a square cylinder by solving directly the compressible Navier-Stokes equations. As the energy of the sound waves generated corresponds to a tiny fraction of the energy of the flow field, the governing equations are discretized using high order numerical schemes to accurately represent the rather different time and spatial scales underlying the physical problem.

The organization of this paper is as follows. Section 2.1 is devoted to describe the flow configuration and the governing equations. The computational domain, grid and the boundary conditions and a description of the numerical procedure used in this work are presented in Section 2.2. Aerodynamics results with some discussions are presented in Section 3.1. The generation mechanisms of sound waves and the effects of the Reynolds and Mach numbers are presented in Section 3.2. Finally, some conclusions are drawn in Section 4.

2. MATHEMATICAL FORMULATION AND NUMERICAL PROCEDURE

2.1 Flow model and parameters

A schematic diagram of the flow model is presented in Fig.1. A square cylinder is fixed at the origin, and the coordinates parallel and normal to the free stream are denoted as x and y, respectively. The Mach number, M, of the uniform flow is defined by $M = U_\infty / c_\infty$. Here, U_∞ denotes the velocity of the uniform flow and c_∞ denotes the speed of sound. The lengths are made dimensionless by the side length D of the cylinder. The velocity is scaled by c_∞, and pressure and stress are scaled by $\rho_\infty c_\infty^2$, where ρ_∞ is the ambient gas density. The Reynolds number is defined as $Re = U_\infty D / \nu_\infty$, where ν_∞ is the kinematic viscosity. In this study, the Reynolds number is prescribed to be $Re = 100, 150$ and 200 and the Mach number to be $M = 0.1, 0.2$ and 0.3. Since the Reynolds number are low, the flow presumably is laminar.
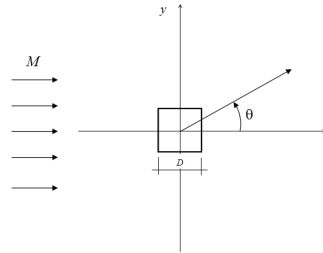

Figure 1. Schematic diagram of the flow model.

The phenomena of generation and radiation of sound waves is governed by compressible Navier-Stokes equations, Eqs. (1) - (5). Since the Mach number is relatively low, temperature dependence of the transport properties is not likely to be a significant effect, Tam et al. (2008). Then, in the energy equation, Eq. (4), viscous dissipation and thermal conduction are neglected, . The energy equation was written in terms of pressure. This facilitates the implementation of boundary conditions in wall regions. Thus, the governing equations may be written as

$$\frac{\partial \rho}{\partial t} + u \frac{\partial \rho}{\partial x} + v \frac{\partial \rho}{\partial y} + \rho \left(\frac{\partial u}{\partial x} + \frac{\partial v}{\partial y} \right) = 0, \tag{1}$$

$$\frac{\partial u}{\partial t} + u \frac{\partial u}{\partial x} + v \frac{\partial u}{\partial y} = -\frac{1}{\rho} \frac{\partial p}{\partial x} + \frac{1}{\rho} \left(\frac{\partial \tau_{xx}}{\partial x} + \frac{\partial \tau_{xy}}{\partial y} \right), \tag{2}$$

$$\frac{\partial v}{\partial t} + u \frac{\partial v}{\partial x} + v \frac{\partial v}{\partial y} = -\frac{1}{\rho} \frac{\partial p}{\partial y} + \frac{1}{\rho} \left(\frac{\partial \tau_{xy}}{\partial x} + \frac{\partial \tau_{yy}}{\partial y} \right), \tag{3}$$

$$\frac{\partial p}{\partial t} + u \frac{\partial p}{\partial x} + v \frac{\partial p}{\partial y} + \gamma p \left(\frac{\partial u}{\partial x} + \frac{\partial v}{\partial y} \right) = 0, \tag{4}$$

where

$$\tau_{xx} = \frac{2M}{Re} \frac{\partial u}{\partial x}, \quad \tau_{xy} = \tau_{yx} = \frac{M}{Re} \left(\frac{\partial u}{\partial y} + \frac{\partial v}{\partial x} \right), \quad \tau_{yy} = \frac{2M}{Re} \frac{\partial v}{\partial y}, \tag{5}$$

and $\gamma = 1.4$ is the ratio of specific heats. The dimensionless velocities in x and in y directions are represented by u and v, respectively. The variables p and ρ denotes the dimensionless pressure and density of the gas, respectively. In order to obtain the aerodynamic and sound fields in the same simulation, the governing equations are solved numerically using high order optimized numerical schemes, which will be described in the next sections.

2.1. Numerical schemes and computational parameters

The simulations are performed by solving the unsteady compressible Navier-Stokes equations in rectangular coordinates, using optimized high order numerical schemes. The spatial derivatives are discretized using low-dispersion and low-dissipation finite-difference schemes, Bogey and Bailly (2004), and Berland et al.(2007): centered 13 points 4th-order finite differences inside the computational domain and reduced to 11, 9 and 7 points 4th-order finite difference as the grid points approximate to the boundaries. Near boundaries, optimized non-centered finite-difference schemes are needed, Tam (1995). The low-storage 4th-order 6th-stage explicit Runge-Kutta algorithm is used to advance de governing equations in time. In order to allow the direct computation of the acoustic field created by the flow, non-reflecting boundary conditions are prescribed at free boundaries, Tam (1993), Bogey and Bailly (2002), and Bogey and Bailly (2004). This type of boundary condition have been conceived such that the sound waves leave the computational domain without significant spurious reflections. On all solid boundaries, the non-slip conditions $u = v = 0$ are imposed, with $\partial p / \partial n = 0$, where n is the direction normal to the rigid surface of the square cylinder. To avoid numerical spurious sound waves due to the low grid resolution, grid stretching, boundary conditions, etc., a set of explicit filters, which is optimized to damp the scales discretized by less than four grid points without affecting the large scales, were applied explicitly to the density, momentum and pressure variables, in every iterations, sequentially in the Cartesian directions, Berland et al. (2007) and Bogey and Bailly (2004). A buffer zone was used in the outflow region to dissipate vortical disturbances before it reach the boundary. This was did by introducing an artificial dissipation term to the right hand side of the governing equations as

$$\frac{\partial \mathbf{q}}{\partial t} + N(\mathbf{q}) = -\sigma_{dp}(x)(\mathbf{q} - \bar{\mathbf{q}}),$$ (6)

where $\mathbf{q}$ is the vector of dependent variables, $N(\mathbf{q})$ a possibly nonlinear operator, $\sigma_{dp}(x)$ is a spatially varying damping coefficient, and $\bar{\mathbf{q}}$ is averaged value of $\mathbf{q}$, about which disturbances are defined. The damping coefficient $\sigma_{dp}(x)$ was selected to blend smoothly between zero in the physical domain and a positive value in the buffer zone.

$$\sigma_{dp} = \frac{1}{2}\beta\{1 + tanh[\alpha_1(x - x_i)]\}\{1 + tanh[\alpha_2(y_i - y)]\}, \quad if \ y \geq 0,$$ (7)

$$\sigma_{dp} = \frac{1}{2}\beta\{1 + tanh[\alpha_1(x - x_i)]\}\{1 + tanh[\alpha_2(y_i + y)]\}, \quad if \ y < 0,$$ (8)

where $\beta = 0.05$, $\alpha_1 = 0.15$, $\alpha_2 = 0.5$, $x_i = 70.0$, $y_i = 10.0$ if $y \geq 0$ and $y_i = -10.0$ if $y < 0$. Figure 2(b) shows the behavior of the $\sigma_{dp}(x)$ along the computational domain and Fig. 2(a) illustrates the effect of the dissipation over the vortical disturbances in the region close to the outflow boundary.

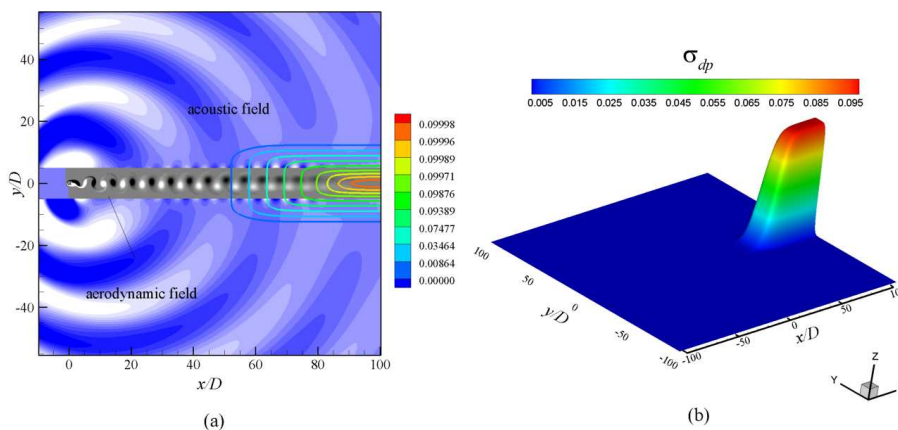(a)   (b)

Figure 2. Application of the buffer zone at the end portion of the computational domain. (a) view of the dissipative effects over the aerodynamic field and (b) smooth distribution of the damping coefficient.

RMS or rms means 'Root Mean Square'.

In this study it was adopted an H-grid system with non-uniform meshes. In order to have a good visualization of the sound field, the length of computational domain was chosen to be $-100 \le x \le 100$ and $-100 \le y \le 100$. The distribution of the grid points along the computational domain was determined in such way that in the range $-1.0 \le x \le 1.0$ and $-1.0 \le y \le 1.0$ a uniform mesh grid was used with 50 points along the side length of the square cylinder. Outside the region of uniform mesh a stretching rate of 0.1 % was used toward the boundary of the computational domain. This yields a total of 953^2 grid points with $\Delta x_{min} = \Delta y_{min} = 0.02$ near wall boundary of the square cylinder and $\Delta x_{max} = \Delta y_{max} = 3.0$ near outer boundary of the computational domain. A sketch of the distribution of the grid points along the computational domain and around the square cylinder can be seen in Fig. 3.
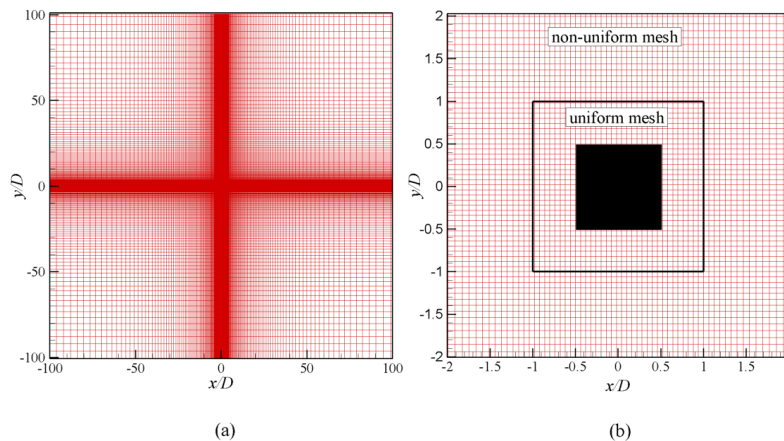
Figure 3. View of the computational mesh. (a) visualization of each 5th points of the H-type grid and (b) close up view of each 3rd points around the square cylinder.

Initial flow fields were given by a uniform flow in the whole computational domain. At the initial stage of time evolution, the wake develops symmetrically with respect to the x-axis. With increased time, the vortex is convected away to the buffer region with decreasing strength due to the viscous effect, and the dies out. Data acquisition for statistics was set sufficiently after of the initial perturbation became negligible.

3. RESULTS

3.1. Aerodynamic results - near field

A typical example of instantaneous flow field is presented in Fig. 4(a) in terms of vorticity for the case of $M = 0.2$ and $Re = 200$. It is important to emphasize that the essential features of the vortex shedding mechanism are the same as those in the circular cylinder case, except that the separation points of the boundary layers on the cylinder surface are fixed at the upstream corners of the square cylinder. The separation of the upper and lower boundary layers from the upstream corners of the square cylinder had been observed in the experiment of Okajima (1982) and in the computation of Sohankar et al. (1998) both for $Re = 150$. The Strouhal number St, in the aeroadynamic field, is better defined by $St = f * D / U_\infty$. The averaged drag coefficient and the Strouhal number are plotted against the Reynolds number in Fig. 5(a) and Fig. 5(b), respectively. It can be seen that the results obtained in the present work are in good agreement with the results of the literature.
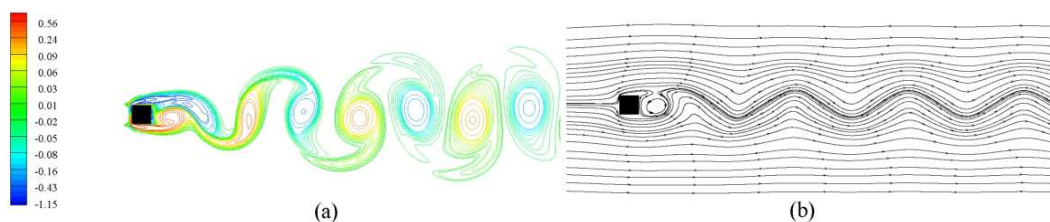
Figure 4. Instantaneous flow field for the case of $M = 0.2$ and $Re = 200$. (a) vorticity and (b) streamlines pattern.
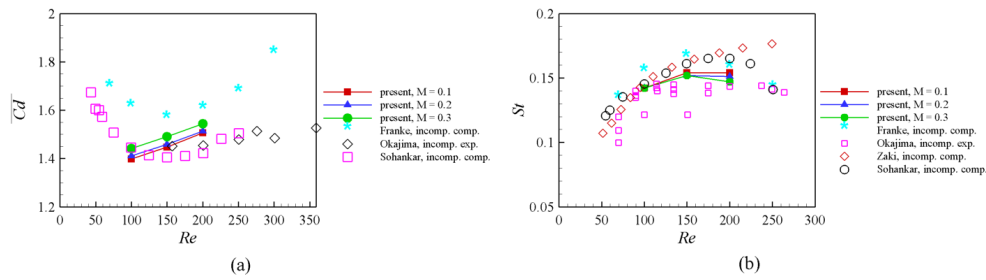
Figure 5. Averaged drag coefficient (a) and Strouhal number (b) vs. Reynolds number. Comparison among the computational results obtained in the present work and results from literature.

Forces acting on the cylinder are presented in Fig. 6 for three different Mach numbers ($M = 0.1, 0.2$ and 0.3), and for three different Reynolds numbers ($Re = 100, 150$ and 200), in terms of lift coefficient Cl and drag coefficient Cd. In the Fig. 6, time variations of Cl and Cd are plotted against the reduced time $t * U_\infty / D - t_p$, where t_p is the time of a peak value. Figure 6 shows that the lift and drag coefficient are not affected significantly by the Mach number, except for $M = 0.3$, where it is possible to note a slight modification in the amplitude and in the phase shift of Cl and Cd signals. Figures 6(a)-(c), show that the averaged drag coefficient $\overline{Cd}$, the RMS values of the lift and drag fluctuations, Cl'_{rms} and Cd'_{rms}, respectively, all increase as the Reynolds number increase. Although the aerodynamics parameters mentioned former present an increase in its values with Reynolds number, the Strouhal number shows a slight modification as the Reynolds number increase. It is important to emphasize the rather difference between the magnitude of the RMS values of lift and drag fluctuations, as can be seen in Fig. 6(b) and Fig. 6(c). This shows that the lift dipole is the main source of sound, which will be analyzed in more detail in the following section.
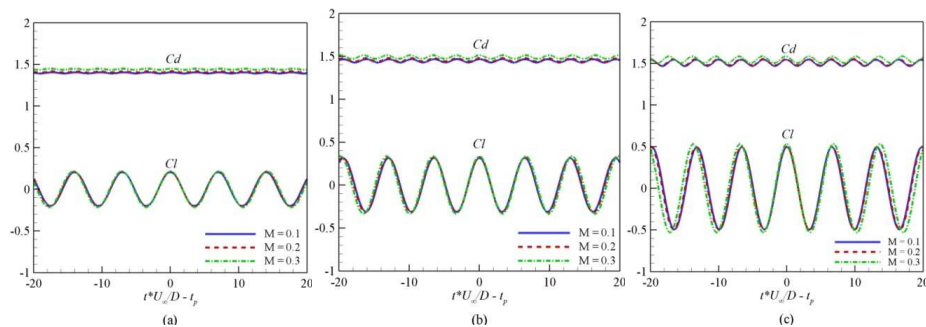

Figure 6. History of draf and lift coefficients for different Mach and Reynolds numbers. (a) Re = 100, (b) Re = 150 and (c) Re = 200.
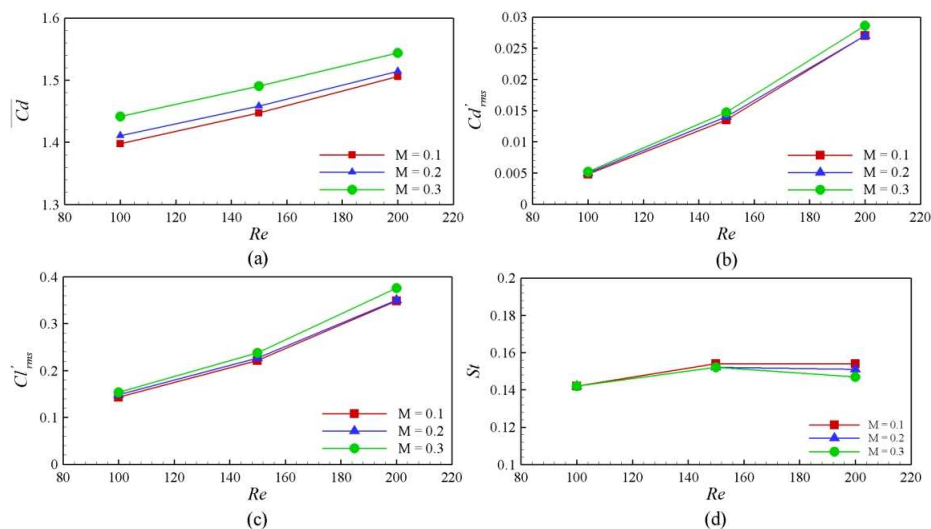

Figure 7. Plot of aerodynamic parameters vs. Reynolds number. (a) averaged drag coefficient, (b) RMS of drag coefficient fluctuations, (c) RMS of lift coefficient fluctuations and (d) Strouhal number.

RMS or rms means 'Root Mean Square'.

3.2. Acoustic results - far field

Sound waves are generated near the surface of the square cylinder in response to the intrinsic unsteady mechanism of vortex shedding. As commented before the amplitude of Cl is much larger than that of Cd, indicating that the intensity of a dipole sound associated with lift force corresponds to the main source of sound in the flow regime studied. The mechanism of sound generation due lift force fluctuation over the cylinder may be understand through Figures 8a and 8b. These figures show a superposition of the acoustic field and flow field in two different times. The acoustic field is visualized using the dilation, $\Theta = \partial u_i / \partial x_i$ and the flow field is visualized using the vorticity. Figure 8a corresponds to the time when Cl takes a maximum value, $t*c_\infty / D = 426.0$ as indicated in Fig. 9. The vorticity field in Fig. 8a shows that a vortex is shed from the upper side of the cylinder in this time. In the same instant a positive sound wave is generated from the upper side of the cylinder and a negative sound wave is generated from the lower side, in response to the vortex shedding. Similarly, Fig. 8b corresponds to the time when the Cl takes a minimum value, $t*c_\infty / D = 438.0$ as indicated in Fig. 9. A vortex is shed from the lower side of the cylinder and a positive sound wave is generated from the lower side and a negative sound wave is generated from the upper side. Therefore, alternate vortex shedding from the upper and lower sides of the cylinder produces positive and negative sound waves alternately from both side of the square cylinder, resulting in a generation of acoustic waves that propagate radially toward the far field.

A time development of the first sound waves generated due to the unsteady computational simulations can be seen in Fig. 10. All time steps correspond to times indicated in Fig. 9. It is important to note the presence of the impulsive sound waves, which were generated due to the uniform flow field used as initial condition. Although the impulsive sound is a potential source of parasite waves, all simulations evolved to a stable solution thanks to the application of the explicit filtering along the computational domain.
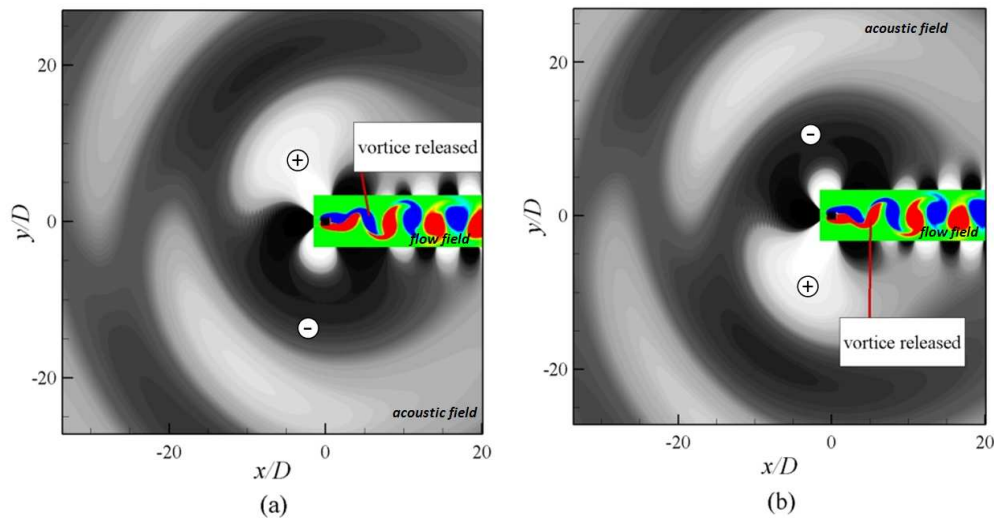

Figure 8. Time development of a flow field and acoustic field. $M = 0.2$ and $Re = 150$. Flow field is visualized by vorticity $(-0.2 \cdots 0.2)$ and acoustic field is visualized by dilatation, $\Theta = \partial u_i / \partial x_i$ $(-1.0 \times 10^{-5} \cdots 1.0 \times 10^{-5})$.

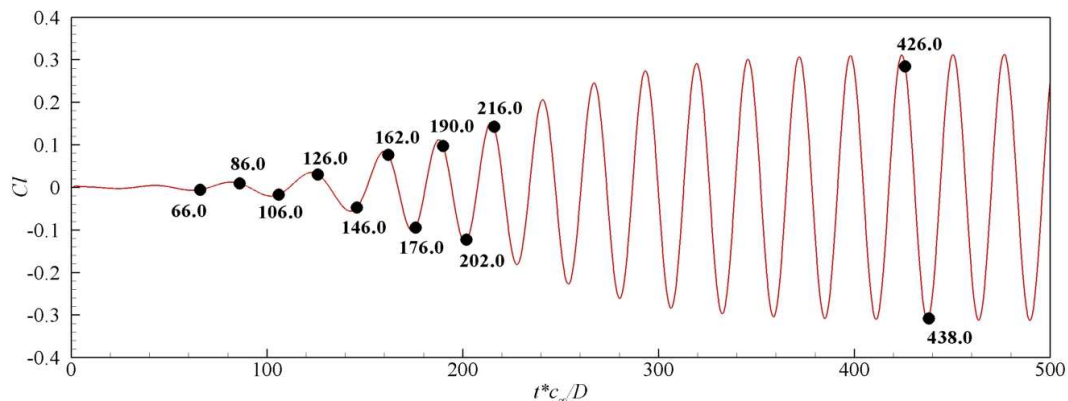(a) $t*c_\infty / D = 426.0$ and (b) $t*c_\infty / D = 438.0$.

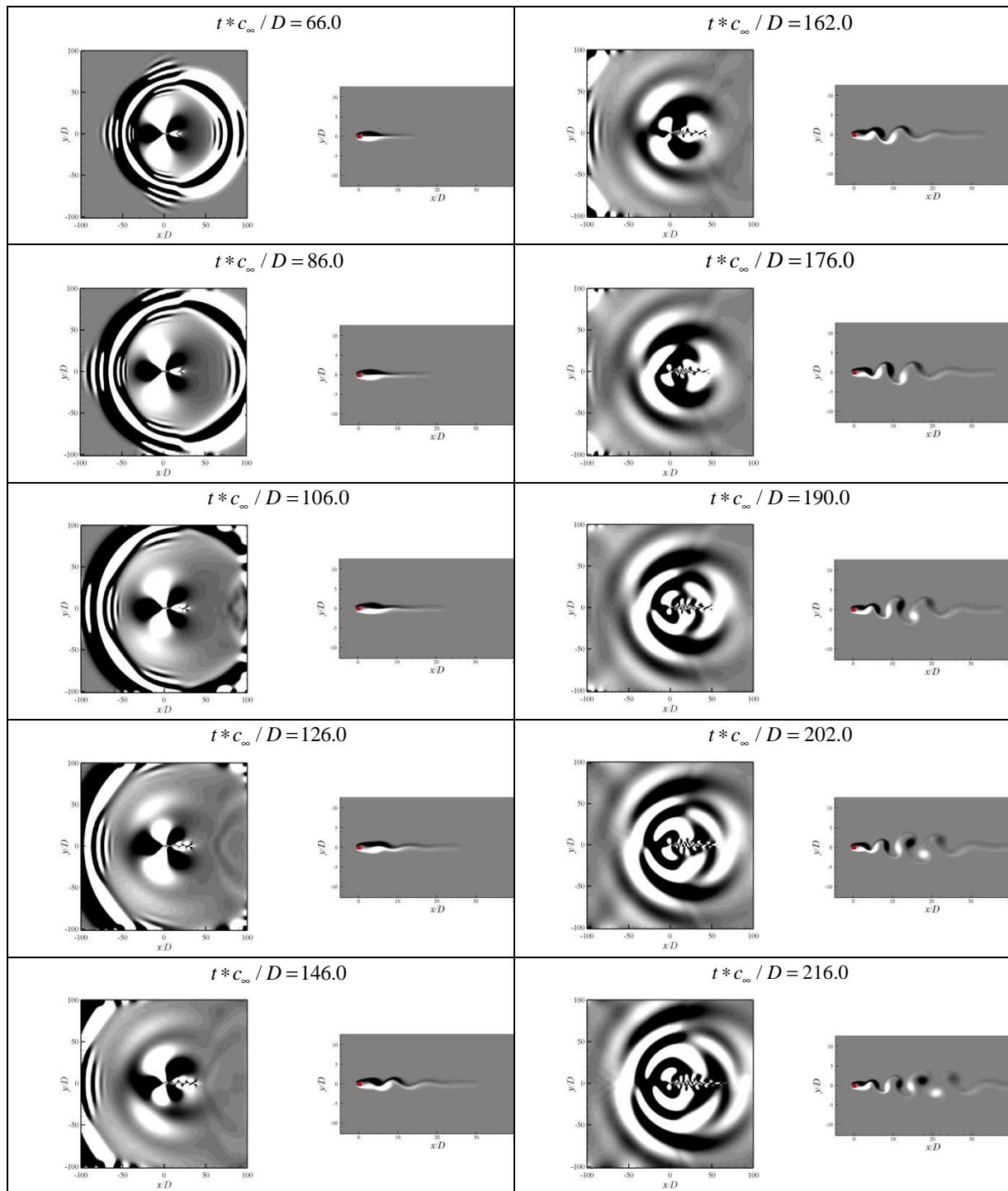Figure 9. Time history of lift coefficient Cl at $M = 0.2$ and $Re = 150$.

Figure 10. Time development of the first sound waves. $M = 0.2$ and $Re = 150$. Dilatation field is visualized to the left and vorticity field to the right.

It is now known that the frequency of the sound is the same as the shedding frequency of vortices from the cylinder into its wake as well as the fluctuation frequency of the lift force, Inoue and Hatakeyama (2002). In order to verify this statement, a sound pressure signal was taken from a probe positioned in the computational domain. The probe was located at $x = 0$, $y = 50$. In Fig. 11. time variations of the sound pressure ($p' = p - \overline{p}$, where $\overline{p}$ is the time averaged pressure) and Cl are plotted against the reduced time $t * c_\infty / D - t_p$, where t_p is the time of a peak value. It can be seen in Fig. 11 that the sound pressure and Cl fluctuation have the same period of oscillation, $\Delta T \cong 33.10$, which shows that the sound pressure has the same frequency of the vortex shedding.
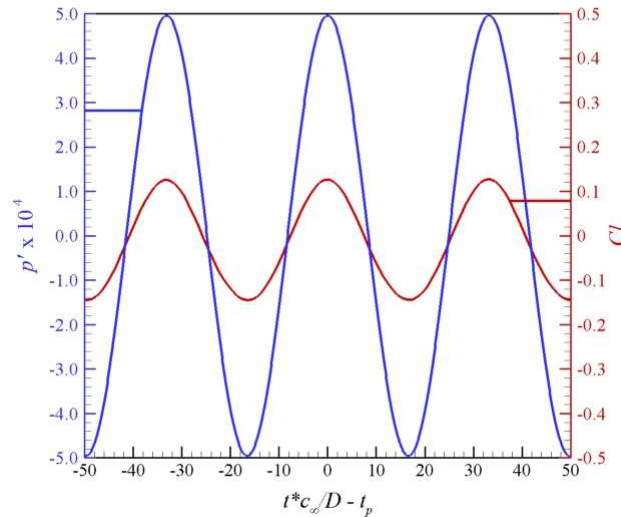
RMS or rms means 'Root Mean Square'.

Figure 11. Time history of the sound pressure and lift coefficient Cl against the reduced time $t*c_\infty / D - t_p$. $M = 0.2$ and $Re = 150$. Sound pressure $p' = p - \bar{p}$ was taken from a probe located at $x = 0, y = 50$. (Remembering that x and y are dimensionless by the characteristic length D).

In contrast to the generation mechanism of the sound in the near field, the nature of the sound in the intermediate and far field is affected by the Mach number. This is mainly due to the Doppler effect. Owing to the Doppler effect, the propagation velocity of the waves is dependent of the angle θ and is described by $c_\theta (\theta) = c_\infty (M \cos \theta - 1)$, at sufficiently small Mach numbers. Then, the sound waves have lower effective propagation velocity upstream and higher downstream. As the wavelength is connected to the effective propagation velocity of the sound waves by $\lambda = c_\theta / f$, sound waves have their wavelengths decreased upstream and increased downstream. This effect is more evident as the Mach number increase, as can be seen in Figs. 12(a-c).
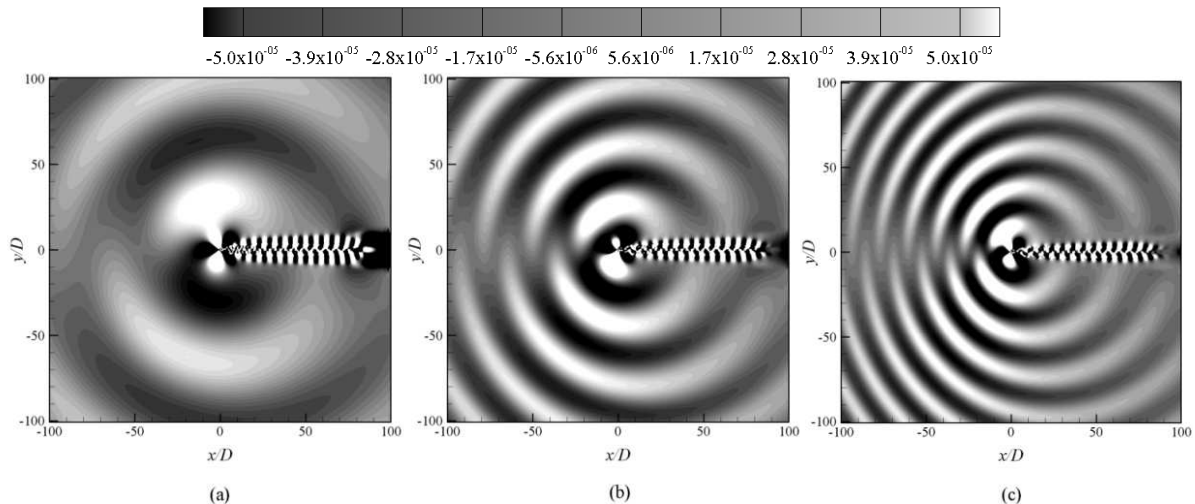

Figure 12 . Snapshot of dilation field for Reynolds number $Re = 200$ and three Mach numbers: (a) $M = 0.1$, the contour levels are from -1.0×10^{-6} to 1.0×10^{-6}, (b) $M = 0.2$, the contour levels are from -1.5×10^{-5} to 1.5×10^{-5} and (c) $M = 0.3$, the contour levels are from -5.0×10^{-5} to 5.0×10^{-5}.

Instantaneous distributions of the dilation $\Theta = \partial u_i / \partial x_i$ are presented against the radial distance in Fig. 13 at $\theta = 90°$, $M = 0.3$ and $Re = 200$. Due to Doppler effect, the propagation velocity of the waves is equal to speed of sound c_∞ at $\theta = 90°$. Figure 13a shows that the acoustic signal decay with increasing distance y (in 2D or radial distance in 3D). Plotted in Fig. 13b are the peak values of the fluctuation pressure against y at $\theta = 90°$. As can be seen from Fig. 13b, the signal peaks tend to decay in proportion to $y^{-1/2}$ with increasing y, in agreement with the theoretical prediction, Inoue and Hatakeyama (2002).
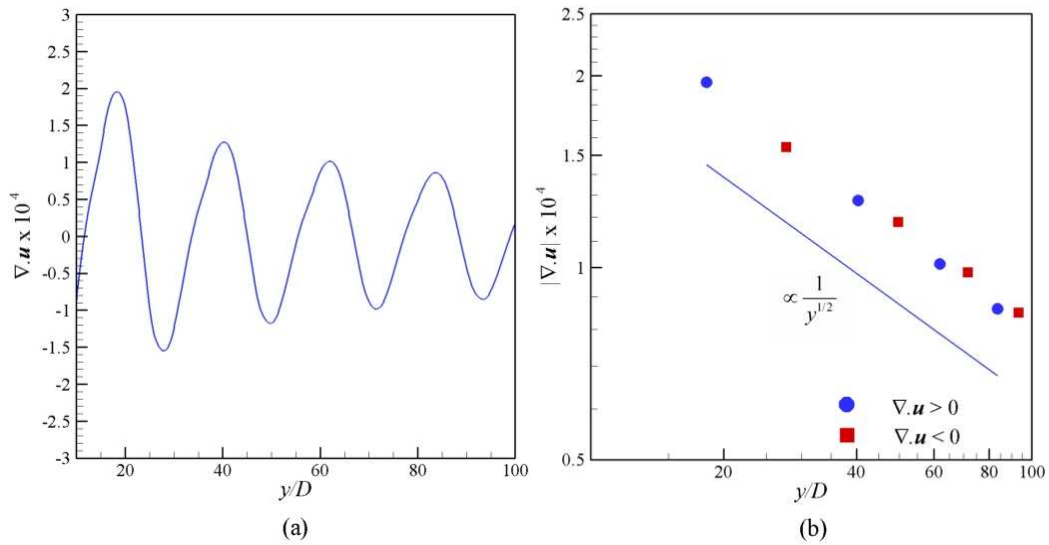
Figure 13. Propagation and decay of the acoustic signal. $M = 0.3$ and $Re = 200$. (a) Propagation of the sound waves shown by mean of the dilatation, $\Theta = \partial u_i / \partial x_i$. (b) Decay of the dilation peaks.

In this study, it can be seen that the sound generated by a flow past a square cylinder is dominated by dipoles, specially by the lift dipole, and the sound field it is characterized by what it is known as aeolian tones. In order to verify this statement different polar plots of the root mean square of the acoustic pressure, p'_{rms}, was obtained at $r = 20$. The Fig. 14 shows that the simulations reproduce the double-lobe curves observed in dipole acoustic fields, Inoue and Hatakeyama (2002). As commented before, the acoustic field is strongly dependent of the Mach number. It can be seen also in Fig. 14 that the acoustic intensity increase with both Mach number and Reynolds number. The effect produced by the Mach number and Reynolds number over the propagation angle is better shown in Table 1. It can be seen that the propagation angle increases with Mach number and decreases with Reynolds number.
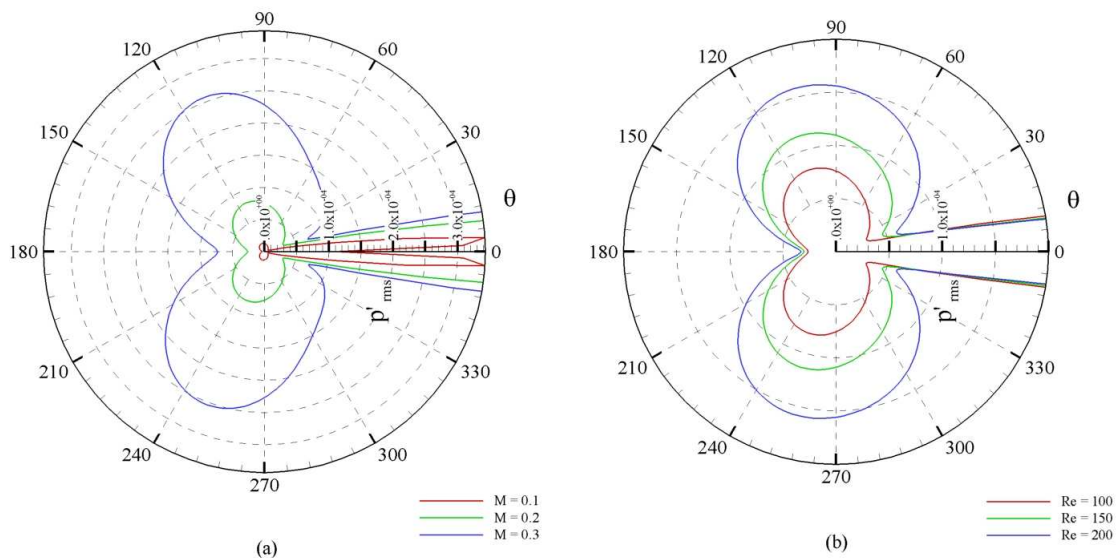

Figure 14. Polar sound pressure directivity at $r = 20$. (a) $Re = 100$ and different Mach numbers. (b) $M = 0.2$ and different Reynolds numbers.

Table 1. Max values of propagation angles and p'_{rms}.

	M = 0.2			Re = 100	
Re	$p'_{rms,max}$	θ_{max}	M	$p'_{rms,max}$	θ_{max}
100	8.099×10^{-5}	108.74°	0.1	1.335×10^{-5}	103.67°
150	1.142×10^{-4}	106.60°	0.2	8.099×10^{-5}	108.74°
200	1.585×10^{-4}	101.12°	0.3	2.571×10^{-4}	111.98°

RMS or rms means 'Root Mean Square'.

In all simulations was observed a shift between a positive sound wave and a negative one, as can be clearly seen in Fig. 15. The straight blue line indicates the propagation direction of a positive sound wave and the straight red line indicates the propagation direction of a negative one. It can be noted that as Reynolds number increases the shift between the positive and negative waves increases. It is possible that this phenomena it is directly related to the increase in drag dipole as Reynolds number increase. Table 2 shows that the angle between the propagation direction of positive and negative sound waves, $\Delta\theta$, increase as the ratio $C'_{l_{rms}} / C'_{d_{rms}}$ decrease, i.e, the contribution of drag dipole increase. However this is not a closed explanation and a further investigation will be necessary to understand whether this is a physical phenomena or just an artifact of the numerical resolution of the governing equations.
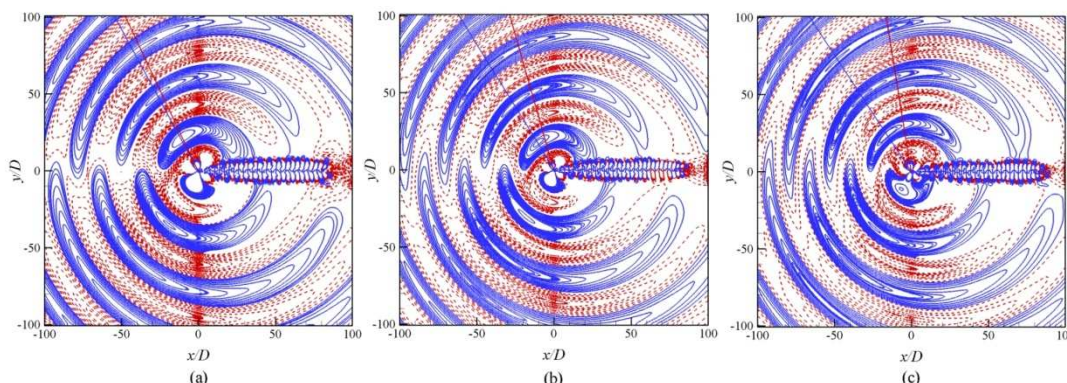

Figure 15. Acoustic field at M = 0.2 and different Reynolds numbers. Blue line corresponds to a positive sound wave and red line to a negative one. (a) Re = 100, $\Delta\theta = 4.21°$, (b) Re = 150, $\Delta\theta = 16.65°$ and (c) Re = 200, $\Delta\theta = 25.79°$.

Table 2. Shift angle and lift and drag coefficients ratio as functions of Reynolds number.

Re	$C'_{l_{rms}} / C'_{d_{rms}}$	$\Delta\theta$
100	29.6	4.21^o
150	16.21	16.65^o
200	12.97	25.79^o

4. CONCLUSIONS

The sound generated by a square cylinder in a flow at M = 0.1, 0.2, 0.3 and Re = 100, 150, 200 has been investigated by direct solution of the two-dimensional unsteady compressible Navier-Stokes equations, and the generation and propagation of the sound waves have been clarified in some detail. The results have shown that sound pressure waves are generated primarily by vortex shedding from the cylinder into its wake. When a vortex is shed from one side of the cylinder, a negative pressure pulse is generated on that side whereas a positive pressure pulse is generated on the other side; alternate vortex shedding from upper and lower sides of the cylinder produces waves on both sides. The generated sound has a dipolar nature and the lift dipole dominates the sound field. The Doppler effect has been shown to affect the propagation process. The Reynolds number has been shown to affect the generation mechanism of sound waves. It has been observed as the Reynolds number increases the shift between positive and negative sound waves became more evident. But a further study is necessary to completely understand this effect.

5. ACKNOWLEGEMENTS

6. REFERENCES

Berland, J., Bogey, C.and Bailly, C., 2006, "Low-dissipation and low-dispersion fourth-order Runge-Kutta alogorithm", Computers & Fluids, Vol. 35, pp. 1459-1463.

Bogey, C. and Bailly, C., 2002, "Three-dimensional non-reflective boundary conditions of acoustic simulations: far field formulation and validation test cases", ACTA Acustica United with Acustica, Vol. 88, pp. 463-471.

Bogey, C. and Bailly, C., 2004, "A family of low dispersive and low dissipative explicit schemes for flow and noise computations", J. Comp. Physics, Vol. 194, pp. 194-214.

Davis, R. W. and Moore, E. F., 1982, "A numerical study of vortex shedding from rectangles", J. Fluid Mech., Vol. 116, pp. 475-506.

Franke, C., Rodi, W.and Shönung, B., 1990, "Numerical calculation of a laminar vortex-shedding flow past cylinders", J. Wind Engng. Ind. Aerodyn., Vol. 35, pp. 237-257.

Inoue, O. and Hatakeyama, N., 2002, "Sound generation by a two-dimensional circular cylinder in a uniform flow", J. Fluid Mech., Vol. 471, pp. 285-314.

Inoue, O. and Suzuki, Y., 2007, "Beat of sound generated by flow past three side-by-side square cylinders", Physics of Fluids, Vol. 19, 048102.

Inoue, O. and Suzuki, Y., 2008, "Beat of sound generated by flow past two side-by-side square cylinder of different sizes", Physics of Fluids, Vol. 20, 076101.

Inoue, O., Iwakami, W. nad Hatakeyama, N., 2006(a), "Aeolian tone radiated from flow past two squarey cylinders in a side-by-side arrangement", Physics of Fluids, Vol. 18, 046104.

Inoue, O., Mori, M., and Hatakeyama, N., 2006(b), "Aeolian tones radiated from flow past two square cylinders in tandem", Fhysics of Fluids, Vol. 18, 046101.

Kninely, C. W., 1990, "Strouhal numbers of rectangular cylinders at incidence: a review and new data", J. Fluids Struct, Vol. 4, pp. 371-393.

Norberg, C., 1993, "Flow around rectangular cylinders: pressure, forces and wakes frequencies", J. Wind Engng. Ind. Aerodyn., Vol. 49, pp. 187-196.

Okajima, A., 1982, "Strouhal numbers of rectangular cylinders", J. Fluid. Mech., Vol. 123, pp. 379-398.

Sohankar, A., Davidson, L. and Norberg, C, 1995, "Numerical simulation of unsteady flow around a square two-dimensional cylinder", Proc. Twelfth Australasian Fluid Mechanics Conf., Sydney, pp. 517-520.

Tam , C. K. W., 1995, "Computational aeroacoustics: issues and methods", AIAA Journal, Vol. 33(10), pp. 1788-1796.

Tam, C. K. W. and Webb, J. C., 1993, "Dispersion-relation-preserving finite difference schemes for computational acoustics", J. Comp. Physics, Vol. 107, pp. 262-281.

Tam, C. K. W., Ju, H. and Walker, B. E., 2008, "Numerical simulation of a slit resonator in a grazing flow under acoustics excitation", J. Sound and Vibration, Vol. 313, pp. 449-471.

Zaki, T. G., Sen, M. and Gad-El-Hak, M., 1994, "Numerical and experimental investigation of flow past a freely rotational square cylinder", J. Fluids Struct., Vol. 8, pp. 555.

7. RESPONSIBILITY NOTICE

The authors are the only responsible for the printed material included in this paper.

RMS or rms means 'Root Mean Square'.